Research

Author for correspondence:
Christopher C. Finlay
e-mail: cfinl@dtu.dk

Satellite monitoring of long period ocean-induced magnetic field variations

Christopher C. Finlay[1], Jakub Velímský[2], Clemens Kloss[1] and Rasmus M. Blangsbøll[1]

[1]Department of Space Research and Technology, Technical University of Denmark, Lyngby, Denmark
[2]Faculty of Mathematics and Physics, Department of Geophysics, Charles University, Prague, Czech Republic

CCF, 0000-0002-4592-2290; JV, 0000-0002-1279-7112; CK, 0000-0001-6899-904X; RMB, 0000-0003-2178-8653

Satellite magnetic field observations have the potential to provide valuable information on dynamics, heat content and salinity throughout the ocean. Here, we present the expected spatio-temporal characteristics of the ocean-induced magnetic field (OIMF) at satellite altitude on periods of months to decades. We compare these to the characteristics of other sources of Earth's magnetic field, and discuss whether it is feasible for the OIMF to be retrieved and routinely monitored from space. We focus on large length scales (spherical harmonic degrees up to 30) and periods from one month up to 5 years. To characterize the expected ocean signal, we make use of advanced numerical simulations taking high-resolution oceanographic inputs and solve the magnetic induction equation in three dimensions, including galvanic coupling and self-induction effects. We find the time-varying ocean-induced signal dominates over the primary source of the internal field, the core dynamo, at high spherical harmonic degree with the cross-over taking place at degrees 13–19 depending on the considered period. The ionospheric and magnetospheric fields (including their Earth-induced counterparts) have most power on periods shorter than one month and are expected to be mostly zonal in magnetic coordinates at satellite altitude. Based on these findings, we discuss future prospects for isolating and monitoring long period OIMF variations using

data collected by present and upcoming magnetic survey satellites.

This article is part of the theme issue 'Magnetometric remote sensing of Earth and planetary oceans'.

1. Introduction

Satellite observations are essential to our modern view of the ocean. They provide global information on circulation patterns [1,2], temperature [3], salinity [4] and biochemistry such as chlorophyll [5] on horizontal scales ranging from 10 to 10 000 km and spanning timescales of weeks to decades, enabling variability and trends in ocean properties to be monitored. These observations are nevertheless heavily focused on the ocean surface; a full understanding of the ocean and its changes also requires information on processes happening at depth. Float programs, in particular ARGO, have in recent years provided much valuable information in this regard [6]. Our knowledge of ocean flows, temperature and salinity as a function of depth nonetheless remains incomplete, especially at depths below 2000 m.

Satellite measurements of gravity and magnetic fields involve an intrinsic integration of ocean properties over depth, so they provide complementary observational constraints on the ocean as a whole. For example, gravity measurements provide constraints on total ocean mass variations and ocean bottom pressure variations which depend on gravity through density integrated over a vertical water column [7]. The GRACE mission has already provided extremely valuable information in this regard, and the upcoming MAGIC mission aims to push such monitoring to higher spatial and temporal resolution [8]. Our focus here is instead on satellite measurements of the magnetic field and the information they can provide on integrated ocean properties on large length scales (of order 1000 km and larger) and long (monthly to decadal) time scales. Magnetic fields are generated by motional induction in the ocean, when electrically conducting water moves across magnetic field lines originating in Earth's core [9–11]. We refer here to such fields as *Ocean-Induced Magnetic Fields* (OIMF), though it is important to note that they also depend on the electrical conductivity of the solid Earth where the induced currents close.

Two classes of oceanic motions contribute to the OIMF. First, and so far best studied, are the magnetic signals due to ocean motions driven by periodic gravitational forcing of the lunisolar tides. Such tidal flows are predominantly two-dimensional, and they give rise to pronounced magnetic signals at the discrete frequencies of the individual tidal constituents [12–14], although nonlinear compound tides also exist [15]. The second class, which is our focus here, involves magnetic signals resulting from the general circulation of the ocean and its dynamics. The latter motions are driven both by winds and buoyancy (also known as thermohaline) effects including surface temperature variations and freshwater release, with timescales ranging from days up to centuries [16–18]. These general circulation motions of the ocean are again largely horizontal, although the small vertical transport plays a crucial role in the dynamics of the thermohaline part of the circulation.

The kinetic energy of near-surface motions is dominated by mesoscale eddies (on length scales of hundreds of kilometres and shorter, and with typical timescales of days to months) [19], however, it is larger (basin-scale) gyres and overturning circulations that dominate thermohaline transport processes over longer timescales. Examples of large-scale ocean currents systems relevant here include the Antarctic Circumpolar Current (ACC), the Atlantic Meridional Overturning Circulation (AMOC) including the Gulf stream, the Indian Ocean Circulation with its Monsoon dynamics, the Pacific Equatorial Currents that are related to the El Niño-Southern Oscillation climate pattern and the North and South Pacific Subpolar Currents including the Kuroshio Current [16,20]. The evolution of these large-scale current systems and their depth variations are of great interest for understanding Earth's climate system [17]. The

OIMF is expected to carry volume-integrated information on such processes, if it can be reliably extracted.

In addition to being dependent on the amplitude and geometry of flows in the ocean, the OIMF also depends on the electrical conductivity of sea water, which in turn depends on temperature and salinity [21,22]. The ocean's electrical conductivity thus varies with geographic location, depth and time, including seasonal variations and long-term trends. Variations in the large-scale OIMF will therefore also be produced by large-scale changes in ocean temperature (i.e. heat content) and salinity.

Over the past decade, there has been significant progress in understanding and simulating the OIMF. There is now consensus regarding the basic features and expected amplitude of the time-averaged OIMF based on advanced simulations that make use of oceanographic data [23]. Simulations suggest the OIMF originates primarily from the upper 2000 m of the ocean where motions are larger and the temperature (hence electrical conductivity) is higher [24]. At Earth's surface and satellite amplitude, it is dominated by the signature of the ACC [25–28]. There is however less consensus regarding the magnetic signal of ocean variability on timescales of months to decades; this depends on the input oceanographic information. For such simulations to be accurate it is important to treat ocean motions, temperature and salinity (as well as the derived electrical conductivity) in a self-consistent manner. This requires input of realistic four-dimensional (three-dimensional plus temporal) ocean properties while acknowledging that even the most up-to-date oceanographic information is incomplete. Systematic numerical experiments are required to address such uncertainties; here, we present only an illustrative example of the OIMF from one such simulation, a more extensive set of simulations is under-way and will be reported in a future study.

Turning to observations of the OIMF, ocean tidal signals can now be routinely extracted from satellite magnetic measurements. The largest and easiest to extract is the M_2 tide [12,29,30] which is available as an L2 Data Product (`SW_MTI_SHA_2C`) from ESA's *Swarm* satellite mission. The magnetic signals of the N_2 and O_1 tides have also been extracted [13,31] and most recently the weaker Q_1 tide (amplitude at satellite altitude of order 0.1 nT) has been convincingly isolated [14]. In the most recent study by Grayver *et al*. [14], spherical harmonic models of the internal magnetic field with a specific period are fit to observations from the CHAMP and *Swarm* satellites, using only night-side data and after correcting for core and magnetospheric fields. The observed OIMF tidal signals agree well with predictions from numerical simulations taking the rather well-known tidal flows as input. These observations of the OIMF tidal signals are an important demonstration that the OIMF can be reliably retrieved from satellite magnetic measurements, despite the small signal amplitude, given appropriate processing and modelling of the signal. Trends in tidal properties, which may reflect trends in temperature, salinity or changes in underlying ocean circulation patterns, are of great interest; this is the next target for studies of the tidal OIMF.

Turning to the more general OIMF signal from the ocean general circulation, as far as we are aware there has only been one published claim to have detected this, based on observations from the CHAMP satellite [32]. This result has however not yet been independently reproduced by other workers. Recently, Hornschild *et al*. [33] sought to make progress by assuming the OIMF signal from a simulation was correct, except for a spatially varying rescaling factor, which they estimated. There is clearly still much to do regarding observational studies of the general circulation-driven OIMF.

The aim of this article is to document the space-time characteristics expected for the general circulation component of the OIMF, and to compare these to other (non-oceanic) magnetic field signals measured by satellites. Based on these comparisons the feasibility of extracting the OIMF will be assessed, and ways to make progress in this direction proposed. In §2, we review the physics of the OIMF, describe how it can be modelled and present its space-time characteristics. In §3, we review the present status of satellite geomagnetism, give an overview of sources of Earth's magnetic field and describe the space-time characteristics of fields originating in the

core, crust, ionosphere and magnetosphere. In §4, we discuss strategies for extracting the OIMF before finishing with discussion and conclusions in §5.

2. Ocean-induced magnetic field

(a) Physics of motional induction

Motion of an electrical conductor through a magnetic field induces an electric field across the conductor. In the presence of a closed conducting path, this results in an electrical current and an associated motionally induced magnetic field. The oceans produce a weak magnetic field in this way as they move through the magnetic field generated in Earth's core.

The OIMF B_{oi} observed, for example, at a satellite at location $(r; t) = (r, \Omega; t) = (r, \vartheta, \varphi; t)$ is an integral property of the electrical current density J_{oi} induced in the oceans, including its closure in the solid Earth. The Biot–Savart law describes this relationship and may be written

$$B_{oi}(r; t) = \frac{\mu_0}{4\pi} \int_G \frac{J_{oi}(r', t) \times (r - r')}{|r - r'|^3} \, dV', \tag{2.1}$$

where $G = G_o \cup G_{se}$ is the volume of the oceans and the solid Earth, taken here to be the region $r \leq a$ where a is the mean spherical radius of Earth's surface and $\mu_0 = \text{const}$ is the magnetic permeability of free space.

The current density $J_{oi}(r; t)$ is specified by Ohm's law for a moving conductor to be

$$J_{oi} = \sigma[(v \times B) + E_{oi}]. \tag{2.2}$$

$J_{oi}(r; t)$ thus depends point-wise on the electrical conductivity $\sigma(r; t)$, the ocean flow velocity $v(r; t)$, the total magnetic field $B(r; t)$ and the electric field $E_{oi}(r; t)$ induced by time changes of the magnetic field. $B(r; t) = B_c(r; t) + B_{oi}(r; t)$ includes both a background magnetic field generated mostly in Earth's core $B_c(r; t)$ and the OIMF $B_{oi}(r; t)$.

The electric field E_{oi}, current density J_{oi} and magnetic field B_{oi} associated with motional induction in the oceans are related by Maxwell's equations. Under the quasi-static approximation that is appropriate for the slow changes considered here, these take the form

$$\nabla \times E_{oi} = -\frac{\partial B_{oi}}{\partial t} \qquad \text{and} \qquad \nabla \times B_{oi} = \mu_0 J_{oi}. \tag{2.3}$$

Combining (2.2) and (2.3) and using the fact that $|B_c| \gg |B_{oi}|$, gives

$$\frac{\partial B_{oi}}{\partial t} = \nabla \times (v \times B_c) - \frac{1}{\mu_0} \nabla \times \left[\frac{1}{\sigma}(\nabla \times B_{oi})\right].$$

Known in magnetohydrodynamics as the magnetic induction equation, this specifies the time evolution of B_{oi} given the ocean flow velocity $v(r; t)$, the electrical conductivity of the oceans and solid Earth $\sigma(r; t)$ and the core field $B_c(r; t)$.

Taking into account the divergence-free condition that holds for all magnetic fields, and an insulating boundary condition at the Earth's surface, we therefore have the following set of equations that can be used to simulate the OIMF:

$$\frac{1}{\mu_0} \nabla \times \left(\frac{1}{\sigma} \nabla \times B_{oi}\right) + \frac{\partial B_{oi}}{\partial t} = \nabla \times (v \times B_c) \quad \text{in } G, \tag{2.4}$$

$$\nabla \cdot B_{oi} = 0 \quad \text{in } G, \tag{2.5}$$

$$B_{oi} = -\nabla U \quad \text{on } \partial G, \tag{2.6}$$

$$\nabla^2 U = 0 \quad \text{in } A, \tag{2.7}$$

5

royalsocietypublishing.org/journal/rsta   Phil. Trans. R. Soc. A **382**: 20240077

$$U = \mathcal{O}(r^{-2}) \text{ as } r \to \infty, \qquad (2.8)$$

$$\boldsymbol{B}_{\text{oi}}|_{t=0} = \boldsymbol{B}_0, \qquad (2.9)$$

where A is the insulating atmosphere $r \geq a$, ∂G is the Earth/atmosphere interface, $U(\boldsymbol{r}; t)$ is the magnetic scalar potential in A, which decreases with radial distance in the absence of external sources and $\boldsymbol{B}_0(\boldsymbol{r}) = \boldsymbol{B}_{\text{oi}}(\boldsymbol{r}; t = 0)$ is the initial condition for the OIMF in G.

The only physical approximation involved in the above equations is the quasi-static approximation of Maxwell's equations, where displacement currents are neglected since low frequencies are considered. Time-dependent electrical conductivities, reflecting changes in the salinity and temperature of the oceans, are permitted. The time derivative of $\boldsymbol{B}_{\text{oi}}$ in the induction equation (2.4) leads to inductive coupling between the highly conductive oceans, the moderately conductive seafloor sediments, and the poorly conductive lithosphere and mantle, as well as self-induction. Spatial variations of electrical conductivity imply the presence of galvanic coupling, as the electric currents prefer the least-resistive path through the heterogeneous medium. This can be demonstrated by writing separately the poloidal and toroidal parts of equation (2.4):

$$\left[\frac{1}{\mu_0}\nabla \times \left(\frac{1}{\sigma}\nabla \times \boldsymbol{B}_{\text{oi}}^{\text{P}}\right)\right]_{\text{P}} + \frac{\partial \boldsymbol{B}_{\text{oi}}^{\text{P}}}{\partial t} = [\nabla \times (\boldsymbol{v} \times \boldsymbol{B}_{\text{c}})]_{\text{P}} - \left[\frac{1}{\mu_0}\nabla \times \left(\frac{1}{\sigma}\nabla \times \boldsymbol{B}_{\text{oi}}^{\text{T}}\right)\right]_{\text{P}}, \qquad (2.10)$$

$$\left[\frac{1}{\mu_0}\nabla \times \left(\frac{1}{\sigma}\nabla \times \boldsymbol{B}_{\text{oi}}^{\text{T}}\right)\right]_{\text{T}} + \frac{\partial \boldsymbol{B}_{\text{oi}}^{\text{T}}}{\partial t} = [\nabla \times (\boldsymbol{v} \times \boldsymbol{B}_{\text{c}})]_{\text{T}} - \left[\frac{1}{\mu_0}\nabla \times \left(\frac{1}{\sigma}\nabla \times \boldsymbol{B}_{\text{oi}}^{\text{P}}\right)\right]_{\text{T}}. \qquad (2.11)$$

The poloidal and toroidal magnetic fields, and corresponding toroidal and poloidal electric currents, are generated respectively by the toroidal and poloidal components of the Lorentz force per unit charge, $\boldsymbol{v} \times \boldsymbol{B}_{\text{c}}$ [34]. Šachl *et al.* [23] have demonstrated that it is important to include galvanic coupling effects when simulating the OIMF by simultaneously modelling both the toroidal and poloidal fields. Equations (2.10) and (2.11) show that lateral variations of electrical conductivity couple the poloidal and toroidal fields, and that energy is exchanged between them.

(b) Numerical simulations

Below we present results from numerical simulations of the OIMF based on a time-domain, spherical harmonic-finite element solver of equations (2.4)–(2.9). The numerical scheme was originally developed to model the electromagnetic response of an electrically heterogeneous Earth to time variations of the magnetic field of external (i.e. magnetospheric or ionospheric) origin [35–37], and later modified to simulate the OIMF by implementation of an internal forcing due to ocean flows [23,34,38].

The magnetic field in G, and the scalar magnetic potential in A are respectively expanded into truncated series of vector and scalar spherical harmonics:

$$\boldsymbol{B}_{\text{oi}}(\boldsymbol{r}; t) = \sum_{j=1}^{J} \sum_{m=-j}^{j} \sum_{\lambda=-1}^{+1} B_{jm}^{(\lambda)}(r; t) S_{jm}^{(\lambda)}(\Omega), \qquad (2.12)$$

$$U(\boldsymbol{r}; t) = a \sum_{j=1}^{J} \sum_{m=-j}^{j} G_{jm}(t)\left(\frac{a}{r}\right)^{j+1} Y_{jm}(\Omega). \qquad (2.13)$$

Here

$$Y_{jm}(\Omega) = \sqrt{\frac{2j+1}{4\pi}\frac{(l-|m|)!}{(l+|m|)!}} P_l^{|m|}(\cos\vartheta) \begin{cases} (-1)^m\sqrt{2}\sin(|m|\varphi) & \text{if } m < 0, \\ 1 & \text{if } m = 0, \\ (-1)^m\sqrt{2}\cos(|m|\varphi) & \text{if } m > 0 \end{cases} \qquad (2.14)$$

are the real, fully normalized scalar spherical harmonics, and the poloidal vertical, toroidal and poloidal horizontal vector spherical harmonics are defined as

$$S_{jm}^{(-1)}(\Omega) = e_r Y_{jm}(\Omega),\tag{2.15}$$

$$S_{jm}^{(0)}(\Omega) = e_r \times \nabla_\Omega Y_{jm}(\Omega),\tag{2.16}$$

$$S_{jm}^{(+1)}(\Omega) = \nabla_\Omega Y_{jm}(\Omega),\tag{2.17}$$

respectively. The magnetic field is further parameterized in the radial direction using piecewise-linear finite elements over the radial coordinate discretized by $0 = r_1 < r_2 < \cdots < r_P < r_{P+1} = a$,

$$B_{jm}^{(\lambda)}(r;t) = \sum_{k=1}^{P+1} B_{jm}^{(\lambda,k)}(t)\psi_k(r),\tag{2.18}$$

$$\psi_k(r) = \begin{cases} \dfrac{r - r_{k-1}}{r_k - r_{k-1}} & \text{for} \quad r \in [r_{k-1}, r_k], \\[2ex] \dfrac{r_{k+1} - r}{r_{k+1} - r_k} & \text{for} \quad r \in [r_k, r_{k+1}], \\[1ex] 0 & \text{elsewhere.} \end{cases}\tag{2.19}$$

An integral formulation of (2.4), a Galerkin scheme applied over the spatial coordinates and a Crank-Nicolson time-integration scheme are then used to construct a linear system of equations. The initial condition $\boldsymbol{B}_0$ is chosen to be the solution of the stationary limit of equation (2.4), found by setting $\frac{\partial \boldsymbol{B}_{oi}}{\partial t}(\boldsymbol{r};0) = \boldsymbol{0}$; this is equivalent to the homogeneous Neumann initial condition. The linear system is assembled and solved using MPI parallelization in the time coordinate, where each node is assigned a contiguous block of time levels, and a full-time series of $\boldsymbol{B}_{oi}(\boldsymbol{r};t)$ is obtained by BiCGStab(2) matrix-free iterations. BiCGStab(2) is a Biconjugate Gradient Stabilized method where a generalized minimal residual step follows every two biconjugate gradient steps. The implementation we employ here, known as elmgTD_mpi, uses a fast matrix-vector product based on Gauss-Legendre quadrature and fast Fourier transform in lateral coordinates, and a preconditioner derived from a simplified problem with radially symmetric conductivity $\sigma_0(r)$ to accelerate the convergence of the iterations.

The simulation of the OIMF presented below is based on daily mean velocities from the ocean state estimate ECCOv4r4 [39,40], which is the latest version of the Estimating the Circulation and Climate of the Ocean framework. Here, we consider only the time interval 2013–2017 that overlaps with the lifetime of *Swarm* satellite mission that is presently surveying the geomagnetic field. ECCOv4r4 seeks to adequately fit global-scale observational constraints on the ocean state [40] (including sea level, temperature profiles, salinity profiles, sea surface temperature, sea surface salinity, sea ice concentration, ocean bottom pressure and mean dynamic topography), while being a solution to a suitably adjusted oceanic general circulation model, the MITgcm [41,42]. More precisely, the adjoint of the MITgcm is used to estimate time-varying atmospheric forcing fields, the model's initial conditions in January 1992 and the model's time-invariant ocean mixing parameters. These are then used in a forward run of the MITgcm from 1992 to 2017 which maintains dynamical and kinematic consistency with the equation of motion and conservation equations.

The three components of $\boldsymbol{v}(\boldsymbol{r};t)$ from ECCOv4r4 are interpolated laterally to the elmgTD_mpi computation grid of 180×360 points, which uses the Gauss-Legendre quadrature nodes in colatitude, and a regular step in longitude. The ocean radial discretization of 50 layers, with layer thicknesses ranging from 10 m close to the ocean surface to 456.5 m in the deepest layer, is carried over to the elmgTD_mpi solver. Below 6134.5 m, which is the maximum depth of ECCOv4r4, zero velocities are prescribed and no forcing is present. The core field $\boldsymbol{B}_c(\boldsymbol{r};t)$ is taken from the spherical harmonic-based IGRF-13 model [43], including its linear secular variation, evaluated on the same grid as the ocean velocity.

The electrical conductivity model $\sigma(\boldsymbol{r}; t)$ is assembled from three sources. In the oceans, the objectively analysed conductivity climatology from collocated salinity and temperature measurements of the World Ocean Atlas (WOA13, [44]) is interpolated to the computation grid using bi-linear interpolation in lateral coordinates and conductance-preserving vertical interpolation. Temporal variations of the ocean conductivity are taken into account by using the WOA13 conductivity monthly means. We acknowledge that the climatological conductivities used here are not fully consistent with the dynamics of the ECCOv4r4 ocean flows; in future work, we plan to compute ocean conductivities more directly from the ocean model's temperature and salinity via an equation of state. Immediately below the seafloor or below the continental surface, a simplified sediment model based on assigned conductivity values for ocean, coastal and continental sediments and maps of their respective thicknesses is used [45]. Again, bi-linear lateral and conductance-preserving vertical interpolation is applied. Finally, below a depth of 26 km, the electrical conductivity follows a one-dimensional profile `MIN_1 DM_0501`, which is constrained by joint inversion of magnetospheric and tidal signals observed by the *Swarm* satellites [46]. In total, the oceans are spanned by 50 layers with four-dimensional spatial and temporal conductivity variations, on a grid consistent with that used for the $\boldsymbol{v} \times \boldsymbol{B}_{\mathrm{c}}$ forcing term, while the sediments are discretized by 40 layers with spatially three-dimensional, time-invariant conductivity and the mantle and core cover 116 one-dimensional layers, with thickness gradually increasing with depth.

(c) Global diagnostics

Below we make use of the following global diagnostics to characterize the typical spatial and temporal scales of the simulated OIMF, and compare these with other expected geomagnetic signals, which are presented in detail below.

To document the power in the magnetic field as a function of spatial lengthscale, we employ the Lowes–Mauersberger spherical harmonic power spectra R_j [47,48]. This is the mean squared vector magnetic field associated with spherical harmonic degree j, which can be computed as

$$R_j = \frac{(j+1)(2j+1)}{4\pi}\left(\frac{a}{r}\right)^{(2j+4)} \sum_{m=-j}^{j} |G_{jm}|^2, \tag{2.20}$$

where G_{jm} are the fully normalized spherical harmonic coefficients of the scalar magnetic potential U.

To characterize the temporal distribution of power as a function of frequency, we consider the median power spectral density $\hat{P}_{B_r}$ of the radial component of the magnetic field $B_r(\boldsymbol{r}; t)$, evaluated on an approximately equal area grid at the radius of interest. We compute the power spectral density using Welch's method [49], and define $\hat{P}_{B_r}$ such that

$$\hat{P}_{B_r}(f_n) = \mathrm{Med}\left\{ \frac{L}{Q}\left[\frac{1}{L}\sum_{q=0}^{L-1} B_r(t_q)W(q)e^{-2iqn/L}\right]^2 \right\}, \tag{2.21}$$

where the input series at each gridpoint is $B_r(t_q)$, f_n are the discrete frequencies at which the power spectra density is estimated, L is chosen to be the length of the time series since we are interested in periods comparable to that of the full-time series. $W(q) = \sin^2(\pi q/L)$ is a Hann window weighting function, $Q = 1/L\sum_q W^2(q)$ and $i = \sqrt{-1}$. Med denotes the median of the power spectral densities computed at each gridpoint on the spherical surface. When the signal considered is the OIMF, a mask is employed so only grid points within or above the ocean are considered.

(d) Filtering

To study the OIMF signal, and other geomagnetic signals, at different spatial scales we truncate the spherical harmonic expansion at chosen minimum or maximum degrees J. For $J \gg 1$ the lengthscale associated with spherical harmonic degree J on a sphere of radius r is approximately $2\pi r/J$.

We investigate different temporal scales filtering in time so as to highlight particular period bands of interest. We first remove the mean value and then use a forward–backward implementation of a 2nd-order Butterworth filter (so the combined action of the filter is 4th order and the filter is by construction zero phase). Initial conditions are set following the method of Gustafsson [50] in order to minimize warm-up transients.

(e) Simulated ocean-induced magnetic field

In this section, we present the global characteristics of the general circulation OIMF signal simulated using the method described above. Results are presented at an altitude of 450 km, a typical altitude of the *Swarm* magnetic survey satellites, which since 2013 have provided high-quality global measurements of the geomagnetic field (see §3 for more details). We focus here on the radial field component.

Figure 1 presents maps of the radial component of the OIMF at 450 km, simulated using the method described above, for the illustrative epoch of 2016.5. It shows the full, unfiltered in time, signal (figure 1*a*), and the signal that is restricted to an annual period band, defined here to be 240–540 days (figure 1*b*). At satellite altitude, the amplitude of the basic OIMF signal is estimated to be of order 1 nT while the annual signal has amplitude of order 0.1 nT, consistent with previous estimates [23,28].

The unfiltered OIMF is most prominent in the Southern oceans, particularly in the Southern Pacific south-east of South America and in the Southern Indian Ocean, both associated with the powerful ACC system. This first-order structure is seen at all times and reflects the time-averaged ocean general circulation. The spherical harmonic power spectra of the OIMF signal at satellite altitude, presented in figure 2, shows this ACC-dominated time-averaged OIMF signal (black curve is the unfiltered OIMF) has peaks in the spherical harmonic power spectra at degrees 2–3 and 6–7.

If one filters the OIMF signal in time so as to remove the time-average, signals from other parts of the ocean become more apparent. For example, in figure 1, we also present a map in 2016.5 of the radial component of the OIMF at satellite altitude, but filtered to highlight a period passband around 1 year (240–540 days). Here, weaker but highly coherent signals are evident, particularly in the Pacific and Indian oceans. The signals in the Pacific have a clear east–west aligned structure and change sign with latitude; three clear changes in the sign of B_r are visible. Given their orientation, it seems likely that these are associated with seasonal variations in the Pacific Equatorial currents and the North and South Pacific currents that are located around latitudes 40 degrees north and south of the equator [16]. Similar signals are also evident in B_r over the Indian ocean. Current systems in the Indian ocean are known to possess strong seasonal variations related to the Monsoon wind system [16]. There also seem to be some smaller-scale, meridionally oriented features, for example, east of central Africa and south of Japan, that given their location may be related to the Somali and the Kuroshio current systems.

Spatial power spectra of the OIMF at satellite altitude, unfiltered (black curve) and filtered to highlight interannual (540–1800 days), annual (540–240 days), semi-annual (240–120 days), monthly (120–30 days) and sub-monthly (<30 days) period bands, are presented in figure 2. Aside from peaks present at degrees 2–3 and 6–7 in the unfiltered spectra, these generally show a power law decrease with increasing degree that reflects field sources located near to Earth's surface (recall ocean depths of up to 6 km are much smaller than the 450 km from Earth's surface to satellite altitude). Re-plotting these spatial spectra at Earth's spherical reference
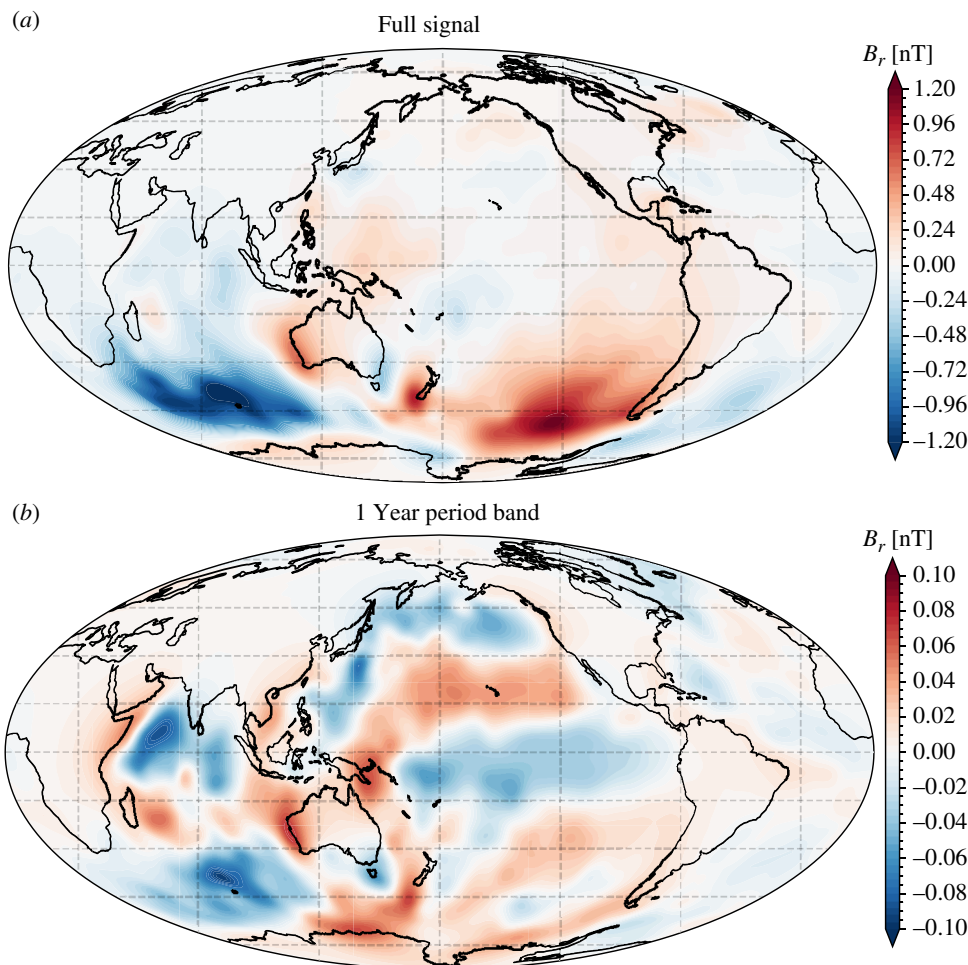
Figure 1. Map of the radial component of the simulated OIMF at satellite altitude, 450 km, unfiltered in time (*a*) and filtered to retain a period band centred on 1 year (*b*), passband 240–540 days, in epoch 2016.5. The spherical harmonic expansion was truncated at degree 60.

radius (not shown), we find that they decrease in power much more slowly, dropping by about one order of magnitude between degrees 5 and 60; the remaining slope is a consequence of the organization of electrical current sources below the ocean surface. Periods shorter than 30 days are found to possess the majority of the variability in the simulated OIMF. The peak power moves to higher spherical harmonic degree as the period shortens. When interpreting these spatial spectra it should be remembered that they involve the temporal spectrum being integrated over period bands of physical significance that are however not uniformly spaced, see the coloured bands in figure 3; the spatial spectra for the shorter periods are also smoother as they effectively involve more complete time-averaging over the considered 5 years.

Turning to the median temporal power spectral density of the radial component of the OIMF at satellite altitude, $\hat{P}_{B_r}(f_n)$ in figure 3 we see that this shows most power per unit frequency at long periods with power decreasing as the period shortens down to 30 days; beyond this the power spectral density is flatter between 30 and 10 days before dropping off steeply below 10 days in this simulation. A similar pattern is seen for all length scales (shown by the spectral densities for different spherical harmonic bands), except for that above degree 18 where we find the power increases for periods between 10 and 30 days, likely associated with mesoscale eddy signatures. There are clear spectral peaks in the simulated OIMF at 1 and 0.5 years associated with annual and semi-annual variations. When comparing the spatial and temporal spectra it
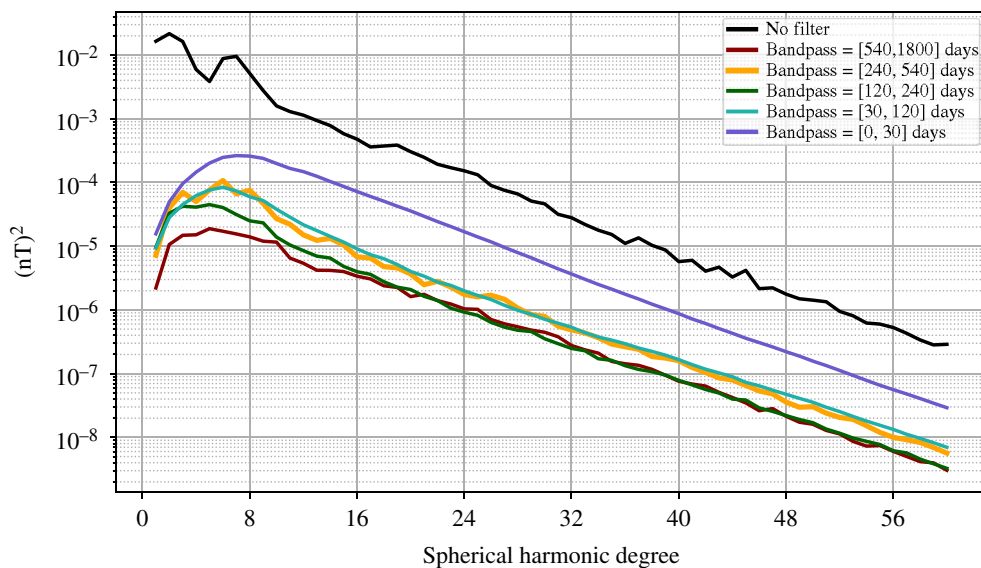
Figure 2. Spatial spectra of the mean squared vector magnetic field of the simulated OIMF as a function of spherical harmonic degree, at altitude 450 km, averaged over time interval 2013.0–2018.0. For the unfiltered in time signal (black) and in interannual, annual, semi-annual, monthly and sub-monthly period bands (colours, see legend).
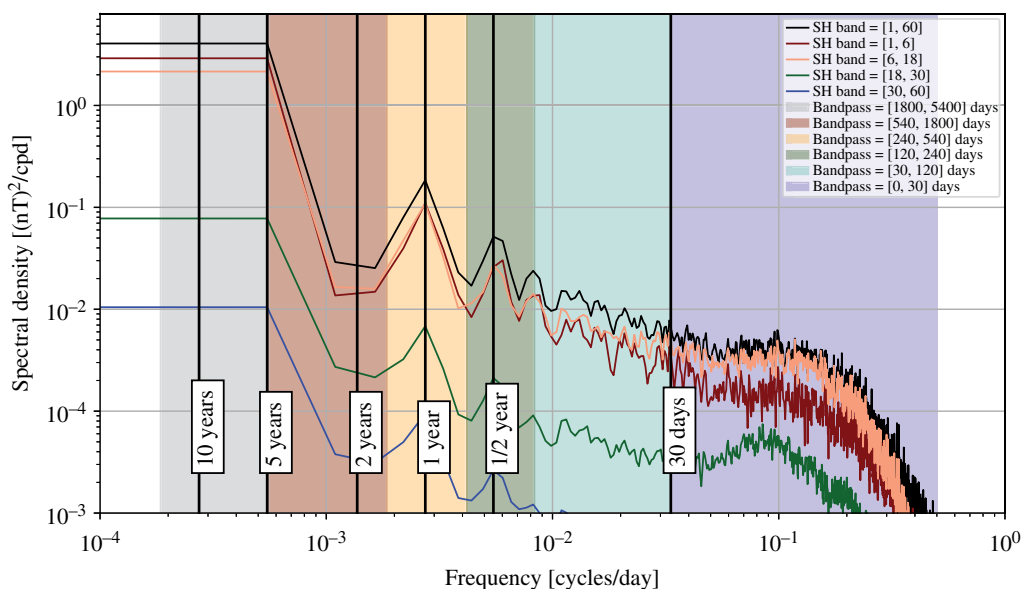

Figure 3. Temporal power spectral density of the simulated radial component of the OIMF at satellite altitude, 450 km. Shown here is the median of power spectra computed on an approximately equal area grid of 3000 points, retaining only locations above the ocean (2095 points). The power spectral density was computed using the Welch method, based on the simulated time interval from 2013.0 to 2018.0. Each solid line shows the spectra from a different range of spherical harmonics degrees, with the black line including all degrees up to 60. The shaded regions indicate the period ranges considered in the spatial spectra. Note the use of log–log axis.

should be remembered that our temporal power spectra densities have been plotted using a log scale in frequency, a consequence of which is that there are far fewer sampled frequencies at low periods. When specific period bands are considered in the spatial spectra, the applied temporal filtering involves weighted sums in the frequency domain. Since there are many more

frequency bins to sum over for the bands at shorter periods, the overall signal in these bands is large, despite the power spectral density at these frequencies being lower.

Note that global averaging is inherent in all the above spectral diagnostics. This may obscure interesting regional OIMF signatures. Regional analysis of the OIMF signal can easily be performed using our analysis tools, but we postpone such investigations to future studies.

3. Satellite geomagnetism

(a) Satellites dedicated to surveying Earth's magnetic field

Having outlined the expected spatial and temporal characteristics of the OIMF at satellite altitude, we now turn to the question of retrieving this signal from magnetic field measurements made by satellites dedicated to surveying Earth's magnetic field. We begin by discussing the available measurements.

Beginning in the late 1960s, pioneering efforts in surveying Earth's magnetic field from space were made by NASA. The POGO satellites provided the first global measurements of field intensity before the short-lived Magsat mission in 1979/1980 delivered the first vector field measurements from space. Since 1999 the past 25 years have seen a series of satellite missions that have surveyed the Earth's magnetic field with increasing accuracy. The Danish Ørsted satellite, launched in 1999, inaugurated this modern era of satellite geomagnetism. Its vector field measurement system, with attitude information supplied by a non-magnetic star tracker co-located with a three-axis fluxgate magnetometer, was calibrated to absolute accuracy using an independent scalar magnetometer measuring the field intensity. The Argentine SAC-C satellite provided scalar intensity measurements from an Ørsted-like payload. The German CHAMP satellite which flew from 2000 to 2010 built on the Ørsted satellite's measurement principles, but provided observations from lower altitudes of 310–450 km, closer to internal field sources including the ocean. Since 2013 ESA's *Swarm* satellite trio has been providing high-quality measurements of the vector magnetic field with absolute accuracy. Launched in 2013, *Swarm* consists of three identical satellites, a lower pair (*Swarm* A and C) flying at altitudes 450–500 km and an upper satellite (*Swarm* B) typically about 50 km higher than the lower pair and drifting in local time. The *Swarm* mission has already provided a decade of high-quality data for studying Earth's magnetic field. The Chinese CSES-1 satellite has provided useful scalar intensity measurement at mid and low latitudes since 2018. Most recently the Macau Scientific Satellite (MSS-1), that like *Swarm* measures the vector field with absolute accuracy, has been launched into a low inclination orbit that complements *Swarm*'s polar orbits with a faster local time coverage at mid and low latitudes. Taken together, we presently have 25 years of high-quality measurements of Earth's magnetic field from low-Earth-orbit. Table 1 summarizes the key characteristics of these magnetic survey satellites.

(b) An overview of geomagnetic field sources

Measurements of Earth's magnetic field made by the low-Earth-orbit satellites described above consist of a superposition of signals from natural current sources present in the Earth's interior and in near-Earth geospace. The largest source is powerful electrical currents generated by turbulent convection that acts as a dynamo in Earth's liquid metal outer core. Close to Earth's surface, in the lithosphere, it is sufficiently cold for a small percentage of minerals to exist in a ferrimagnetic form which allows microscopic currents to be organized into large-scale magnetizations of geological structures that together give rise to the crustal or lithospheric field. Also near to Earth's surface are the electrical currents induced by the motions of the ocean that are the primary focus here.

Table 1. Summary of satellite missions carrying absolute scalar magnetometers and used for geomagnetic field modelling.

mission	dates	altitude (km)	inclination (°)	magnetometer
POGO	1965–1971	400–1500	82–87	scalar only
Magsat	1979–1980	350–450	97	vector and scalar
Ørsted	1999–2013	650–850	97	vector and scalar
CHAMP	2000–2010	310–450	97	vector and scalar
SAC-C	2001–2004	698–705	97	scalar only[a]
Swarm A, B and C	2013–	450–550	87, 88 and 87	vector and scalar
CSES-1	2018–	~500	97	scalar only[a]
MSS-1	2023–	~450	41	vector and scalar

[a]Payload included vector magnetometer, data not typically used for field modelling.

Moving further out into the atmosphere, strong currents exist in the Ionospheric E-region around 110 km altitude. High conductivity of the atmosphere due to ionization on the dayside and thermally and gravitationally driven motions (including solar and lunar tides) give rise to the Solar quiet (Sq) current system in this region. The Sq current system moves with the sun and is modulated by seasonal variations in Earth's orbit and by solar activity. In the high latitude ionosphere, there are highly dynamic auroral electrojet current systems fed by field-aligned currents that originate primarily in the night side of the outer magnetosphere (the magnetotail). These field-aligned currents are also known as magnetosphere–ionosphere (MI) coupling currents. Electrical conductivity is high in polar regions due to particles hitting the Earth's atmosphere there, being guided by Earth's magnetic field, as seen in auroral displays. Significant currents also exist further out in the magnetosphere, in the radiation belts, in the magnetopause where the solar wind reaches Earth's magnetic field and in the magnetotail on the night side of the Earth. The most important of these for satellite observations in low-Earth-orbit are the currents in the radiation belts, typically at distances of 6–10 times Earth's radius, where circulating charged particles give rise to so-called magnetospheric ring currents. These are dramatically enhanced when energy from solar disturbances is transferred into the magnetosphere following vigorous solar activity. Both magnetospheric and ionospheric currents vary rapidly and hence induce secondary currents in the electrically conducting regions of the Earth, particularly in the ocean, lithosphere and upper mantle.

A simplified cartoon showing the basic geometry of these current systems is shown in figure 4. The real currents are of course much more spatially complex and not steady. Table 2 collects some summary information regarding these sources.

From table 2 the formidable challenge of extracting the OIMF at satellite altitude is immediately apparent. It is small compared to the signals from the other sources. This means that careful selection, modelling and filtering of the data based on the expected properties of both the OIMF and the those of the other sources, must be carried out.

An important aspect of the OIMF is that it is internal to the orbits of the satellites. Using the tools of geomagnetic field modelling, and given good global data coverage, it is possible to separate sources internal and external to the observation altitude. This means the major task in extracting the OIMF is to separate it from other internal sources: the core and the crustal/lithospheric fields, the ionospheric field (i.e. internal to satellites) and its associated Earth-induced fields, and Earth-induced currents driven by magnetospheric field variations. In the sub-sections below, we describe each of these in turn, presenting spatial and temporal characteristics from the state-of-the-art models of each source with the aim of characterizing their properties at satellite altitude and understanding how they might be separated from the OIMF.
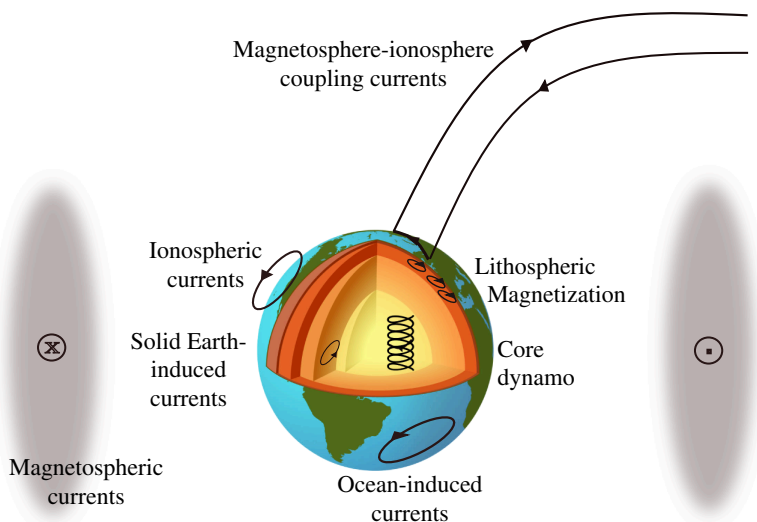
Figure 4. A simplified cartoon depicting major near-Earth electrical current systems that contribute to Earth's magnetic field (not to scale, magnetospheric currents are in reality much more distant and with a complex spatiotemporal structure).

Table 2. Summary of major sources of the near-Earth geomagnetic field. Information on expected length and time scales of the resulting fields at satellite altitude is shown through their spatial and temporal spectra in figures 2, 3 and 5–7.

source	approx. geocentric radius of current system (km)	order of magnitude at satellite altitude (nT)[a]
core dynamo	1220–3840	40 000
crustal/lithospheric magnetization	6300–6371	10
ocean-induced currents	6365–6371	1
solar-quiet (Sq) ionospheric currents	~6480	20
auroral electrojet ionospheric currents	~6480	50
field-aligned MI coupling currents	6480–1 00 000	100
magnetospheric ring current	20 000–60 000	20
Earth-induced currents	3480–6371	10

[a]During geomagnetically quiet times of low solar activity, but note there can be considerably day-to-day variability for external sources.

(c) Core and crustal fields

As is clear from table 2, the core dynamo is by far the largest source of magnetic fields measured close to the Earth. In figure 5, we present time-averaged spatial spectra (left panel) and temporal spectra (right panel) of the core field at satellite altitude (450 km altitude) from a recent Earth-like core dynamo simulation, the 100% path coupled-Earth dynamo [51] whose construction involved the assimilation of geomagnetic observations. The advantage of using a simulation here is that we obtain estimates of the core field's properties for length and time scales shorter than those traditionally considered for the core field, which are relevant for comparisons with the properties of the OIMF, while it also agrees well with traditional geomagnetic field models [43] at larger length scales. Spatial spectra are also shown for the same period bands as considered in figure 2. The spatial spectra of the crustal (or more strictly
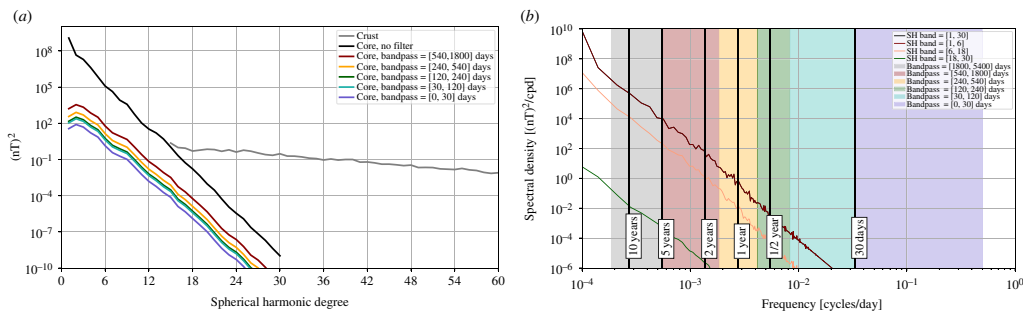
Figure 5. (*a*) Spatial spectra of the mean squared vector magnetic field from a simulation of the core dynamo [51] as a function of spherical harmonic degree, at satellite altitude (450 km). As well as the unfiltered signal (black curve), spatial spectra are shown for interannual, annual, semi-annual, monthly and sub-monthly period bands (coloured curves). The spatial power spectrum of the LCS-1 crustal field model [52] is also shown (grey curve). (*b*) Temporal power spectral density $\hat{P}_{B_r}$ of the simulated radial component from the same core dynamo simulation at satellite altitude, unfiltered and in chosen spherical harmonic bands (curves can overlap). These curves are the median of power spectral densities, computed using a Welch-type method, of time series of B_r computed on an approximately equal area grid of 3000 points at satellite altitude.
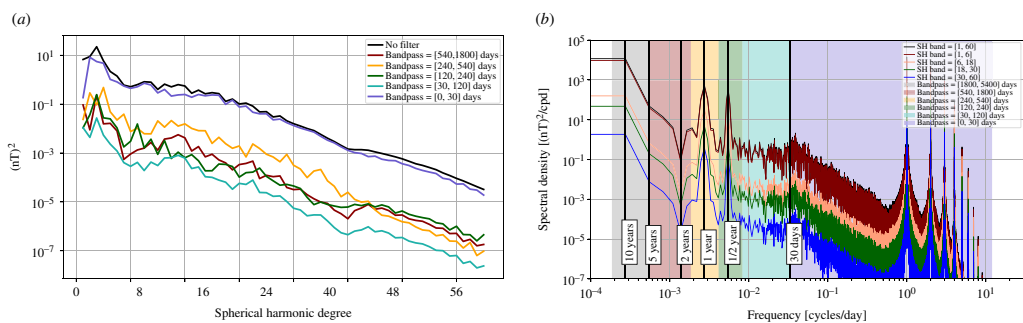

Figure 6. (*a*) Spatial spectra of the mean squared vector magnetic field from the CI ionospheric field [54], v. 9, including its Earth-induced counterpart, as a function of spherical harmonic degree, at satellite altitude (450 km). As well as the unfiltered signal (black curve), spatial spectra are again shown for interannual, annual, semi-annual, monthly and sub-monthly period bands (coloured curves). (*b*) Temporal power spectral density of the radial component of the ionospheric field and associated Earth-induced fields, again from the CI model, version 09, at satellite altitude. This is the median of the power spectral densities computed using a Welch-type method from time series of B_r at 3000 approximately equal area grid points.

the lithospheric) field is also included in figure 5, taken from the LCS-1 [52] model based on observations from the CHAMP and *Swarm* satellite missions.

Although the core field is very strong on large length scales, its spatial spectra at satellite altitude drops off steeply as it is due to an internal source more than 3000 km away. This is the case for all the considered period bands. The temporal power spectral density of the core field at satellite altitude also drops off steeply at all considered spatial wavelengths (up to spherical harmonic degree 30). Compared with the shallower spatial and temporal spectra for the OIMF in figures 2 and 3 it is clear that at sufficiently short length and time scales one should expect the OIMF to dominate over the core field; we discuss this opportunity further in §4.

Turning to the crustal field, like the OIMF this shows a shallower spatial spectrum at satellite altitude, since both are associated with sources close to Earth's surface. However, the crustal field changes only very slowly in time [53]. For the periods below 10 years considered here, time variations in the crustal field are expected to be small. So although it is very difficult to separate the steady component of the OIMF from the crustal field, the time-varying OIMF on periods of 10 years and shorter should not be significantly polluted by the crustal field.

(d) Ionospheric and associated Earth-induced fields

Figure 6 presents similar spatial and temporal spectra at satellite altitude from an observation-based model of ionospheric field and its associated Earth-induced counterparts. The model employed is the *Swarm* comprehensive inversion [54], CI, version 09, which represents E-layer currents, with a specific focus on the Sq system, including explicit estimates of daily variations and related higher harmonics, annual and semi-annual variations, as well as solar modulation through a dependence on F10.7 solar flux. The associated Earth-induced currents are calculated based on a three-dimensional model of ocean and sediment electrical conductivity above a one-dimensional conducting mantle [55].

The spatial spectra shown for different passbands in figure 6 illustrate that the majority of the ionospheric and related induced signal occurs on timescales shorter than 30 days. The temporal power spectral densities show distinct lines at 1 day and harmonics on all the investigated lengthscales. Considering timescales longer than 30 days, much of the ionospheric signal can therefore be filtered out.

There are however significant ionospheric signals remaining in both the annual and semi-annual period bands; these are much larger than the annual and semi-annual signals seen in the temporal spectra for the simulated OIMF in figure 3. Note that the spectra shown in figure 6 are based on the modelled global ionospheric and induced fields each hour between 2014.0 and 2024.0, including both the day and night sides. The amplitudes of the Sq currents will be weaker on the night side; we discuss these issues further in §4.

We have not explicitly considered field-aligned magnetospheric–ionospheric coupling currents here. Although of large amplitude, these are expected to be of short length scale and to vary rapidly in time. They are associated with toroidal magnetic fields, so should be orthogonal to poloidal fields of internal origin such as the OIMF. They will however have an indirect impact through the E-layer currents they drive in the polar regions; although these are, in principle, included in the CI model we have employed here, its parameterization is not optimized for the polar region.

(e) Earth-induced fields driven by magnetospheric sources

Finally, we turn to the field induced in the conducting Earth by variations of magnetospheric currents. Here, we do not explicitly consider the magnetospheric field itself, since we assume it can be adequately separated from the internal field by potential field modelling. To characterize the magnetospheric induced field we have used the CHAOS-7 [56] magnetospheric field model, which includes a parameterization of the near-Earth magnetospheric ring current with time-dependence given by the ground-based RC index, and a simple treatment of fields due to magnetopause and magnetotail currents [57] capturing daily and annual variations related to changes in geocentric-solar-magnetic coordinates with respect to the Earth-fixed-Earth-Centered frame [58]. This was used as the inducing field and the induced response of the conducting Earth was computed in the time-domain using the method of Grayver [59] again using a three-dimensional ocean and sediment electrical conductivity model above a one-dimensional electrically conducting mantle [46]. Spatial and temporal spectra of the resulting internal induced field are presented in figure 7.

The spatial spectra of the internal Earth-induced field produced by magnetospheric variations are dominated by large length scales and most of the power occurs on periods less than 30 days. The temporal power spectral density does nevertheless show power across all frequencies though without the very strong spectral lines found for the ionospheric field (the weak lines in figure 7 on daily and high harmonics are artefacts due to a restriction to night-side ground observatories applied when computing the RC index). There are nevertheless noticeable spectral peaks at annual and especially semi-annual periods that are likely related to variations of the Earth's orbital plane with respect to the solar wind and associated variations
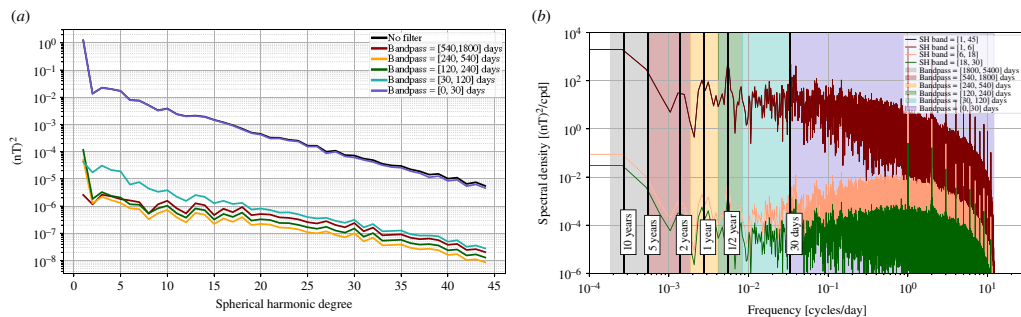
Figure 7. (*a*) Spatial spectra of the mean squared vector magnetic field at satellite altitude (450 km) associated with Earth-induced internal currents produced by magnetospheric variations from the CHAOS-7 magnetospheric field model [56] acting on a three-dimensional ocean + one-dimensional mantle conductivity model, calculated using the method of Grayver [59] and averaged over 2014.0 to 2024.0. As well as the unfiltered signal (black curve), spatial spectra are shown for interannual, annual, semi-annual, monthly and sub-monthly period bands (coloured curves). (*b*) Temporal power spectral density $\widehat{P}_{B_r}$ at satellite altitude of the radial component of the same Earth-induced internal field, unfiltered (black) and in chosen spherical harmonic bands (curves can overlap). These curves are the median of power spectral densities, computed using a Welch-type method from time series of B_r computed on an approximately equal area grid of 3000 points at satellite altitude.
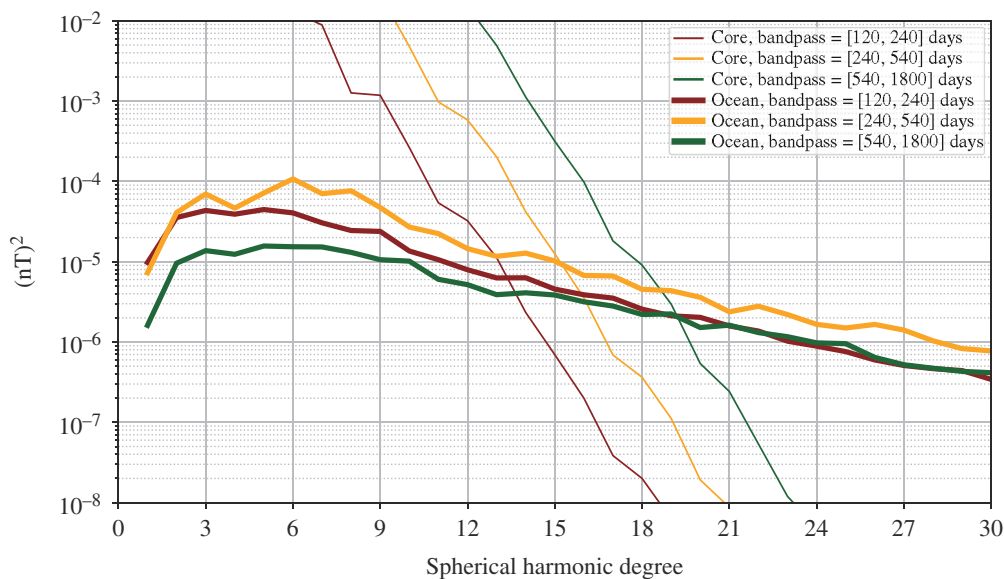

Figure 8. Comparison of spatial spectra of the oceanic induced and core magnetic fields, at satellite altitude (450 km), up to spherical harmonic degree 30. The spectra cross, so that the ocean signal dominates above degrees 13−19 depending on the period considered.

in magnetospheric current systems as seen on the Earth [60–62]. The power present at annual and semi-annual periods in the magnetospheric variations (and also the ionospheric variations presented previously) is clearly much larger than the OIMF signals at these periods. Methods for separating out large external scale fields (e.g. resulting in the green and orange lines in figure 7*b*) are clearly essential if the OIMF field is to be extracted.

As for the ionospheric field, these results have been computed from a global internal (induced) field each hour, without selecting geomagnetically quiet times. It therefore includes geomagnetic storms for which significant induced fields are expected. Focusing on geomagnetic
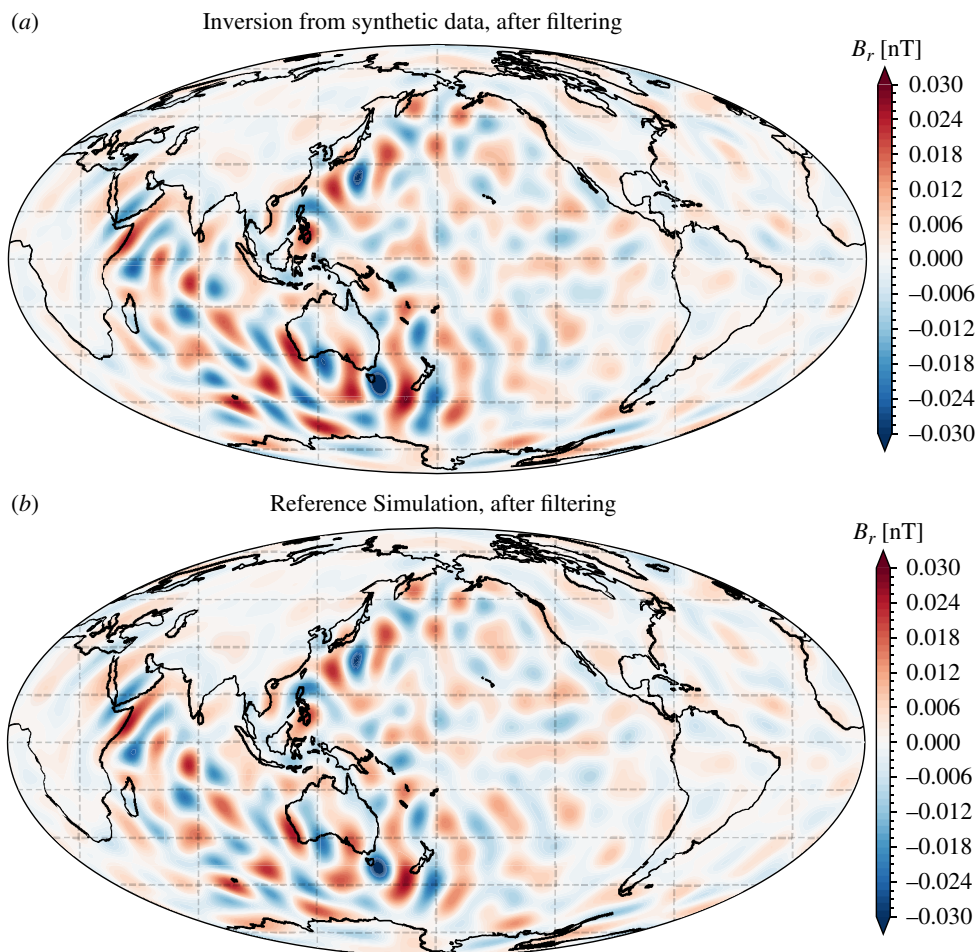
(*a*) Inversion from synthetic data, after filtering

(*b*) Reference Simulation, after filtering

Figure 9. Map of the radial component of the OIMF at satellite altitude (450 km), filtered to retain a period band centred on 1 year (passband 240–540 days) and spherical harmonic degrees 16–30. (*a*) Result from inversion of synthetic satellite data. (*b*) For reference, simulated OIMF used to generate the synthetic satellite data.

quiet times a weaker magnetospheric induced signal is expected, we return to this question in the next section.

4. Strategies for extracting the OIMF

Based on the above characteristics of the various geomagnetic field sources at satellite altitude, we now discuss possible strategies for extracting the OIMF signal.

Given the dominant role of the core field in the near-Earth magnetic field, an obvious first question is whether the OIMF is always obscured below the core field. In figure 8, we present comparisons of the spatial power spectra for the core and ocean-induced signals at satellite altitude, considering the semi-annual (120–240 days), annual (240–540 days) and interannual (540–1800 days) period bands. We find the OIMF spectra cross the core fields spectra at degrees 13–19; the crossing takes place at lower degree for shorter periods. This suggests that we should expect the OIMF to dominate over the core field signal on short length scales and short time scales, for example, at spherical harmonic degrees greater than 15 for annual periods. Recall that considering the annual period band the signal due to the nearly steady crustal field should also be negligible.
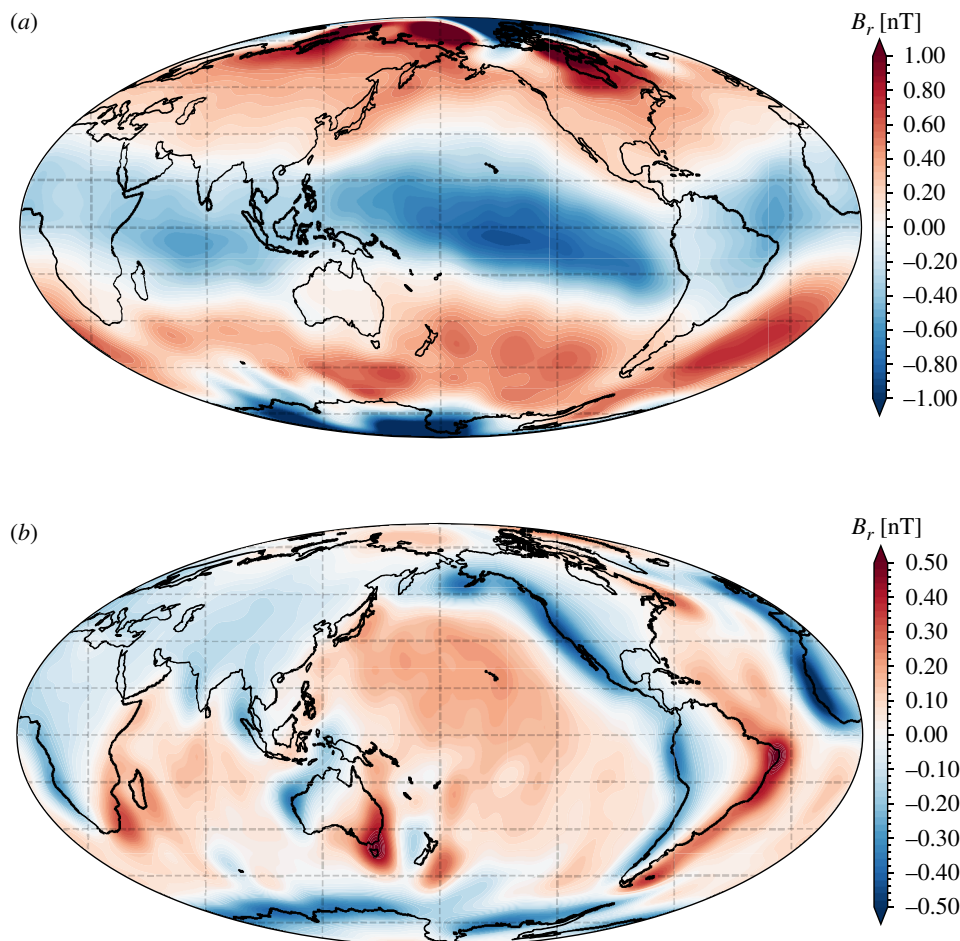
Figure 10. (*a*) Ionospheric and associated induced field in the annual period band, estimated by inversion of synthetic satellite data from dark/night regions, based on the CI v. 9 model [54]. Radial field is shown at 450 km altitude, up to spherical harmonic degree 30 in 2016.5. (*b*) Magnetospheric induced internal field in the annual period band, at 450 km altitude, up to spherical harmonic degree 30 in 2016.5, based on the CHAOS magnetospheric model [56] acting on a three-dimensional ocean conductivity and sediments model with an underlying one-dimensional conducting Earth [22].

To further test this hypothesis, we carried out a field modelling experiment, evaluating our simulated core field and OIMF along the actual orbits of the *Swarm* A, B and C satellites between 2014.0 and 2024.0. We applied geomagnetic quiet-time and dark selection criteria, and used vector and vector gradient data at non-polar latitudes, scalar intensity data in the polar region, and scalar gradients at all latitudes, similar to the CHAOS-7 model [57]. We inverted for a time-varying internal field up to spherical harmonic degree 30 and parameterized time-dependence using cubic splines with a 0.15 year knot spacing. The resulting radial field at satellite altitude, filtered to show the signal in the 1 year period band, and only spherical harmonic degrees 16–30, is presented in figure 9, along with the input OIMF signal for reference. We are clearly able to successfully retrieve the OIMF signal from degree 16 to 30 in this 1 year period band, despite the presence of a realistic core field. Physically interesting signals are evident especially in the equatorial Pacific (likely associated with westward wave propagation) and in the Indian ocean (related to monsoon-driven seasonal variations in the ocean circulation).

This synthetic test is however incomplete as we have ignored the additional fields related to ionospheric and magnetospheric sources. Figure 10 shows the results of similar inversions carried out based on synthetic satellite data containing only the ionospheric and associated

induced signals (figure 10*a*), and only the magnetospheric induced signals (figure 10*b*). Unlike the results shown in the earlier sections, these inversion results now take into account the dark and geomagnetic quiet-time conditions that are important for assessing the impact of magnetospheric and ionospheric signals when estimating internal field signals.

Both the magnetospheric induced signal and the ionospheric and associated induced signals estimated in these inversions are much larger than the OIMF signal in the annual period band, even when considering dark and geomagnetically quiet conditions. However, both are rather large scale, at least outside the polar region (for the ionospheric field) and away from the ocean continent boundaries (the magnetospheric induced field). A simple approach to isolating the OIMF might therefore involve spatially filtering to remove these magnetospheric and ionospheric components. For example, by excluding spherical harmonic degrees below 16 (already necessary to exclude the core field) and possibly also the low order (near zonal) part of the field. Such crude filtering will, of course, also remove OIMF signals of interest and may not even be sufficient to remove all the ionospheric and magnetospheric fields. A better approach will certainly be to make use of ionospheric and magnetospheric field models, such as those we have used here for our synthetic tests, removing their predictions from the satellite data before they are used in field modelling.

5. Discussion and conclusions

Using models for the different contributions to Earth's magnetic field we have shown that the long period OIMF is measurable at satellite altitude and that it dominates over the core field signal provided one considers sufficiently short length and time scales.

The general circulation OIMF field signal at such length and time scales, for example, at spherical harmonic degree above 15 in the annual period band, is however expected to be rather small on the basis of the models considered here, on the order of 0.02 nT. The most serious obstacles to retrieving this signal are ionospheric and associated Earth-induced fields, and Earth-induced fields driven by magnetospheric field variations, both of which, like the OIMF, are internal to satellite orbits. Our tests suggest that these are associated with rms signals of order of 0.15 and 0.05 nT, respectively, at satellite altitude, for spherical harmonic degrees 16–30 in the annual period band; these means 90% and 50% respectively of these signals would need to be corrected or filtered out in order for the OIMF to be retrieved.

Progress towards meaningful satellite magnetic monitoring of the OIMF will require that these confounding signals are sufficiently well-modelled and removed from satellite data before inverting for the OIMF. It is not the day-to-day variability of the magnetospheric and iono-spheric signals that it is crucial here, rather their slow variations on the monthly to decadal timescales of interest for the OIMF. Inversion strategies such as regularization at Earth's surface, or use of prior model covariances based on the expected fields from advanced OIMF simula-tions could also help. The application of filters during post-processing that are designed to remove remaining signal of ionospheric and magnetospheric origin will also likely be essential.

The geomagnetic models we have employed here involve some known limitations. Polar ionospheric fields are not fully described in the CI model and we have effectively ignored field-aligned currents. Our characterizations will therefore underestimate the complexity of real geomagnetic data in the polar region. For this reason, we recommend that investigations of the OIMF should focus, at least to begin with, on signals at mid and low latitudes. For example, our simulations suggest the existence of locally strong signals in the Indian Ocean in the annual period band. The numbers quoted above for the typical OIMF and magnetospheric/ionospheric field amplitudes are global rms values; it might be significantly easier to extract the OIMF in particular locations. There are also limitations in our knowledge of the mantle electrical conductivity, in particular in its deep three-dimensional structure. Depending on the true mantle conductivity the magnetospheric induced field could be more complex than that we have investigated here, however, deep mantle structures are expected to primarily impact the

observed field on large lengthscales. It should also be acknowledged that the investigations presented above were based on a single advanced OIMF simulation, there are uncertainties in the ocean flows and the conductivity structures that serve as its inputs. The true OIMF could therefore also differ from that presented here, although experience with the tidal OIMF suggests simulations of the type considered here should be fairly reliable guides [14].

Despite the challenges described above, we believe that detecting the OIMF due to ocean dynamics is now feasible and worth a concerted effort by the geomagnetic community. Magnetic remote sensing of ocean dynamics would provide valuable independent constraints on ocean dynamics, and has the potential to eventually contribute, along with other observations, to our knowledge of changes in ocean heat content and deep salinity variations.

The past decade with continuous magnetic field observations from the three *Swarm* satellites have seen important advances in our modelling of ionospheric and magnetospheric fields. These will be further improved in the upcoming years thanks to the data from the MSS-1 satellite and its successors, and the planned NanoMagSat satellites, which will provide much improved local time coverage from space. With *Swarm* also descending closer to the ocean sources during the next solar minimum there could be a bright future ahead for magnetic remote sensing of ocean dynamics, but it still remains to be demonstrated with real observations that the long period OIMF signal can be reliably extracted.

References

1. Wunsch C, Stammer D. 1998 Satellite altimetry, the marine geoid, and the oceanic general circulation. *Annu. Rev. Earth Planet. Sci.* **26**, 219–253. (doi:10.1146/annurev.earth.26.1.219)
2. Knudsen P, Andersen O, Maximenko N. 2021 A new ocean mean dynamic topography model, derived from a combination of gravity, altimetry and drifter velocity data. *Adv. Space Res.* **68**, 1090–1102. (doi:10.1016/j.asr.2019.12.001)
3. Merchant CJ *et al.* 2019 Satellite-based time-series of sea-surface temperature since 1981 for climate applications. *Sci. Data* **6**, 223. (doi:10.1038/s41597-019-0236-x)
4. Boutin J *et al.* 2021 Satellite‑based sea surface salinity designed for ocean and climate studies. *J. Geophys. Res.* **126**, e2021JC017676. (doi:10.1029/2021JC017676)

5. Hu C, Lee Z, Franz B. 2012 Chlorophyll *a* algorithms for oligotrophic oceans: a novel approach based on three‑band reflectance difference . *J. Geophys. Res.* **117**. (doi:10.1029/2011JC007395)

6. Roemmich D, Gilson J. 2009 The 2004–2008 mean and annual cycle of temperature, salinity, and steric height in the global ocean from the argo Program. *Prog. Oceanogr.* **82**, 81–100. (doi:10.1016/j.pocean.2009.03.004)

7. Hughes CW, Williams J, Blaker A, Coward A, Stepanov V. 2018 A window on the deep ocean: the special value of ocean bottom pressure for monitoring the large-scale, deep-ocean circulation. *Prog. Oceanogr.* **161**, 19–46. (doi:10.1016/j.pocean.2018.01.011)

8. Daras I *et al.* 2024 Mass-change and geosciences international constellation (MAGIC) expected impact on science and applications. *Geophys. J. Int.* **236**, 1288–1308. (doi:10.1093/gji/ggad472)

9. Sanford TB. 1971 Motionally induced electric and magnetic fields in the sea. *J. Geophys. Res.* **76**, 3476–3492. (doi:10.1029/JC076i015p03476)

10. Tyler RH, Mysak LA. 1995 Electrodynamics in a rotating frame of reference with application to global ocean circulation. *Can. J. Phys.* **73**, 393–402. (doi:10.1139/p95-055)

11. Minami T. 2017 Motional induction by tsunamis and ocean tides: 10 years of progress. *Surv. Geophys.* **38**, 1097–1132. (doi:10.1007/s10712-017-9417-3)

12. Tyler RH, Maus S, Lühr H. 2003 Satellite observations of magnetic fields due to ocean tidal flow. *Science* **299**, 239–241. (doi:10.1126/science.1078074)

13. Saynisch-Wagner J, Baerenzung J, Hornschild A, Irrgang C, Thomas M. 2021 Tide-induced magnetic signals and their errors derived from CHAMP and Swarm satellite magnetometer observations. *Earth. Planets. Space* **73**, 1–11. (doi:10.1186/s40623-021-01557-3)

14. Grayver AV, Finlay CC, Olsen N. 2024 Magnetic signals from oceanic tides: new satellite observations and applications. *Phil. Trans. R. Soc. A* **382**, 20240078. (doi:10.1098/rsta.2024.0078)

15. Einšpigel D, Martinec Z. 2017 Time-domain modeling of global ocean tides generated by the full lunisolar potential. *Ocean Dyn.* **67**, 165–189. (doi:10.1007/s10236-016-1016-1)

16. Talley L, Pickard GL, Emery WJ, Swift JH. 2011 *Descriptive physical oceanography: an introduction*. Amsterdam, The Netherlands: Elsevier Press. (doi:10.1016/B978-0-7506-4552-2.10001-0)

17. Williams RG, Follows MJ. 2011 *Ocean dynamics and the carbon cycle*. Cambridge UK: Cambridge University Press. (doi:10.1017/CBO9780511977817)

18. Wunsch C. 2015 *Modern observational physical oceanography: understanding the global ocean*. Princeton, NJ: Princeton University Press.

19. Chelton DB, Schlax MG, Samelson RM. 2011 Global observations of nonlinear mesoscale eddies. *Prog. Oceanogr.* **91**, 167–216. (doi:10.1016/j.pocean.2011.01.002)

20. Steele JH, Thorpe SA, Turekian KK. 2009 *Ocean currents*. Boston, MA: Academic Press.

21. Millero FJ. 2010 History of the equation of state of seawater. *Oceanography* **23**, 18–33. (doi:10.5670/oceanog.2010.21)

22. Grayver AV. 2021 Global 3‑D electrical conductivity model of the world ocean and marine sediments. *Geochem. Geophys. Geosyst.* **22**, e2021GC009950. (doi:10.1029/2021GC009950)

23. Šachl L, Martinec Z, Velímský J, Irrgang C, Petereit J, Saynisch J, Einšpigel D, Schnepf NR. 2019 Modelling of electromagnetic signatures of global ocean circulation: physical approximations and numerical issues. *Earth. Planets. Space* **71**. (doi:10.1186/s40623-019-1033-7)

24. Irrgang C, Saynisch-Wagner J, Thomas M. 2018 Depth of origin of ocean-circulation-induced magnetic signals. *Ann. Geophys.* **36**, 167–180. (doi:10.5194/angeo-36-167-2018)

25. Stephenson D, Bryan K. 1992 Large‑scale electric and magnetic fields generated by the oceans. *J. Geophys. Res.* **97**, 15467–15480. (doi:10.1029/92JC01400)

26. Vivier F, Maier‑Reimer E, Tyler RH. 2004 Simulations of magnetic fields generated by the Antarctic circumpolar current at satellite altitude: can geomagnetic measurements be used to monitor the flow? *Geophys. Res. Lett.* **31**, L10306. (doi:10.1029/2004GL019804)

27. Glazman RE, Golubev YN. 2005 Variability of the ocean‑induced magnetic field predicted at sea surface and at satellite altitudes. *J. Geophys. Res.* **110**, C12. (doi:10.1029/2005JC002926)

28. Manoj C, Kuvshinov A, Maus S, Lühr H. 2006 Ocean circulation generated magnetic signals. *Earth. Planets. Space* **58**, 429–437. (doi:10.1186/BF03351939)

29. Sabaka TJ, Tyler RH, Olsen N. 2016 Extracting ocean‐generated tidal magnetic signals from *Swarm* data through satellite gradiometry . *Geophys. Res. Lett.* **43**, 3237–3245. (doi:10.1002/2016GL068180)

30. Sabaka TJ, Tøffner-Clausen L, Olsen N, Finlay CC. 2020 CM6: a comprehensive geomagnetic field model derived from both CHAMP and Swarm satellite observations. *Earth. Planets. Space* **72**, 1–24. (doi:10.1186/s40623-020-01210-5)

31. Grayver AV, Olsen N. 2019 The magnetic signatures of the M2, N2, and O1 oceanic tides observed in Swarm and CHAMP satellite magnetic data. *Geophys. Res. Lett.* **46**, 4230–4238. (doi:10.1029/2019GL082400)

32. Golubev Y. 2012 Ocean‐generated magnetic field study based on satellite geomagnetic measurements: 2. Signal inference. *J. Geophys. Res.* **117**, C9. (doi:10.1029/2012JC007976)

33. Hornschild A, Baerenzung J, Saynisch-Wagner J, Irrgang C, Thomas M. 2022 On the detectability of the magnetic fields induced by ocean circulation in geomagnetic satellite observations. *Earth. Planets. Space* **74**, 182. (doi:10.1186/s40623-022-01741-z)

34. Velímský J, Šachl L, Martinec Z. 2019 The global toroidal magnetic field generated in the Earth's oceans. *Earth Planet. Sci. Lett.* **509**, 47–54. (doi:10.1016/j.epsl.2018.12.026)

35. Velímský J, Martinec Z. 2005 Time-domain, spherical harmonic-finite element approach to transient three-dimensional geomagnetic induction in a spherical heterogeneous Earth. *Geophys. J. Int.* **161**, 81–101. (doi:10.1111/j.1365-246X.2005.02546.x)

36. Velímský J. 2013 Determination of three-dimensional distribution of electrical conductivity in the Earth's mantle from Swarm satellite data: time-domain approach. *Earth. Planets. Space* **65**, 1239–1246. (doi:10.5047/eps.2013.08.001)

37. Velímský J, Knopp O. 2021 Lateral variations of electrical conductivity in the lower mantle constrained by Swarm and CryoSat-2 missions. *Earth. Planets. Space* **73**. (doi:10.1186/s40623-020-01334-8)

38. Velímský J, Schnepf NR, Nair MC, Thomas NP. Can seafloor voltage cables be used to study large-scale circulation? An investigation in the Pacific Ocean. *Ocean Sci.* **17**, 383–392. (doi:10.5194/os-17-383-2021)

39. Forget G, Campin JM, Heimbach P, Hill CN, Ponte RM, Wunsch C. 2015 ECCO version 4: an integrated framework for non-linear inverse modeling and global ocean state estimation. *Geosci. Model Dev.* **8**, 3071–3104. (doi:10.5194/gmd-8-3071-2015)

40. Fukumori I, Wang O, Fenty I, Forget G, Heimbach P, Ponte RM. 2021 *ECCO version 4 release 4*. Technical report.

41. Marshall J, Adcroft A, Hill C, Perelman L, Heisey C. 1997 A finite‐volume, incompressible Navier Stokes model for studies of the ocean on parallel computers. *J. Geophys. Res.* **102**, 5753–5766. (doi:10.1029/96JC02775)

42. Adcroft A, Campin JM, Hill C, Marshall J. 2004 Implementation of an Atmosphere–ocean general circulation model on the expanded spherical cube. *Mon. Wea. Rev.* **132**, 2845–2863. (doi:10.1175/MWR2823.1)

43. Alken P, Thébault E, Beggan CD, Nosé M. 2022 Special issue 'International geomagnetic reference field: the thirteenth generation.' *Earth. Planets. Space* **74**, 49. (doi:10.1186/s40623-021-01569-z)

44. Tyler RH, Boyer TP, Minami T, Zweng MM, Reagan JR. 2017 Electrical conductivity of the global ocean. *Earth. Planets. Space* **69**, 156. (doi:10.1186/s40623-017-0739-7)

45. Everett ME, Constable S, Constable CG. 2003 Effects of near-surface conductance on global satellite induction responses. *Geophys. J. Int.* **153**, 277–286. (doi:10.1046/j.1365-246X.2003.01906.x)

46. Grayver AV, Munch FD, Kuvshinov AV, Khan A, Sabaka TJ, Tøffner-Clausen L. 2017 Joint inversion of satellite-detected tidal and magnetospheric signals constrains electrical conductivity and water content of the upper mantle and transition zone. *Geophys. Res. Lett.* **44**, 6074–6081. (doi:10.1002/2017GL073446)

47. Mauersberger P. 1956 Das mittel der energiedichte des geomagnetischen hauptfeldes an der erdoberfläche und seine säkulare änderung. *Gerl. Beitr. Geophys.* **65**, 207–215.

48. Lowes FJ. 1966 Mean-square values on sphere of spherical harmonic vector fields. *J. Geophys. Res.* **71**, 2179–2179. (doi:10.1029/JZ071i008p02179)

49. Welch PD. 1967 The use of fast Fourier transform for the estimation of power spectra: a method based on time averaging over short, modified periodograms. *IEEE Trans. Audio Electroacoust.* **15**, 70–73. (doi:10.1109/TAU.1967.1161901)

50. Gustafsson F. 1996 Determining the initial states in forward-backward filtering. *IEEE Trans. Signal Process.* **44**, 988–992. (doi:10.1109/78.492552)

51. Aubert J. 2023 State and evolution of the geodynamo from numerical models reaching the physical conditions of Earth's core. *Geophys. J. Int.* **235**, 468–487. (doi:10.1093/gji/ggad229)

52. Olsen N, Ravat D, Finlay CC, Kother LK. 2017 LCS-1: a high-resolution global model of the lithospheric magnetic field derived from CHAMP and Swarm satellite observations. *Geophys. J. Int.* **211**, 1461–1477. (doi:10.1093/gji/ggx381)

53. Hulot G, Olsen N, Thébault E, Hemant K. 2009 Crustal concealing of small-scale core-field secular variation. *Geophys. J. Int.* **177**, 361–366. (doi:10.1111/j.1365-246X.2009.04119.x)

54. Sabaka TJ, Tøffner-Clausen L, Olsen N, Finlay CC. 2018 A comprehensive model of Earth's magnetic field determined from 4 years of swarm satellite observations. *Earth. Planets. Space* **70**, 1–26. (doi:10.1186/s40623-018-0896-3)

55. Sabaka TJ, Olsen N, Tyler RH, Kuvshinov A. 2015 CM5, a pre-Swarm comprehensive geomagnetic field model derived from over 12 yr of CHAMP, Ørsted, SAC-C and observatory data. *Geophys. J. Int.* **200**, 1596–1626. (doi:10.1093/gji/ggu493)

56. Finlay CC, Kloss C, Olsen N, Hammer MD, Tøffner-Clausen L, Grayver A, Kuvshinov A. 2020 The CHAOS-7 geomagnetic field model and observed changes in the South Atlantic Anomaly. *Earth. Planets. Space* **72**, 156. (doi:10.1186/s40623-020-01252-9)

57. Olsen N, Lühr H, Finlay CC, Sabaka TJ, Michaelis I, Rauberg J, Tøffner-Clausen L. 2014 The CHAOS-4 geomagnetic field model. *Geophys. J. Int.* **197**, 815–827. (doi:10.1093/gji/ggu033)

58. Laundal KM, Richmond AD. 2017 Magnetic Coordinate Systems. *Space Sci. Rev.* **206**, 27–59. (doi:10.1007/s11214-016-0275-y)

59. Grayver AV, Kuvshinov A, Werthmüller D. 2021 Time-domain modeling of three-dimensional Earth's and planetary electromagnetic induction effect in ground and satellite observations. *J. Geophys. Res. Space Phys.* **126**. (doi:10.1029/2020JA028672)

60. Russell CT, McPherron RL. 1973 Semiannual variation of geomagnetic activity. *J. Geophys. Res.* **78**, 92–108. (doi:10.1029/JA078i001p00092)

61. Malin SRC, Isikara AM. 1976 Annual variation of the geomagnetic field. *Geophys. J. Int.* **47**, 445–457. (doi:10.1111/j.1365-246X.1976.tb07096.x)

62. Malin SRC, Winch DE, Işıkara AM. 2006 Semi-annual variation of the geomagnetic field. *Earth. Planets. Space.* **58**, 321–328. (doi:10.1186/BF03352236)